

Local intraspecific aggregation in phytoplankton model communities: spatial scales of occurrence and implications for coexistence

Coralie Picoche^{1,*}, William R. Young², Frédéric Barraquand^{1,*}

¹Institute of Mathematics of Bordeaux, University of Bordeaux and CNRS, Talence, France

²Scripps Institution of Oceanography, La Jolla, California, USA

Abstract

The coexistence of multiple phytoplankton species despite their reliance on similar resources is often explained with mean-field models assuming mixed populations. In reality, observations of phytoplankton indicate spatial aggregation at all scales, including at the scale of a few individuals. Local spatial aggregation can hinder competitive exclusion since individuals then interact mostly with other individuals of their own species, rather than competitors from different species. To evaluate how microscale spatial aggregation might explain phytoplankton diversity maintenance, an individual-based, multispecies representation of cells in a hydrodynamic environment is required. We formulate a three-dimensional and multispecies individual-based model of phytoplankton population dynamics at the Kolmogorov scale. The model is studied through both simulations and the derivation of spatial moment equations, in connection with point process theory. The spatial moment equations show a good match between theory and simulations. We parameterized the model based on phytoplankters' ecological and physical characteristics, for both large and small phytoplankton. Defining a zone of potential interactions as the overlap between nutrient depletion volumes, we show that local species composition—within the range of possible interactions—depends on the size class of phytoplankton. In large phytoplankton, individuals are surrounded by cells from other species, while in small phytoplankton, individuals remain in mostly monospecific clusters. Spatial structure therefore favours intra- over inter-specific interactions for small phytoplankton, which likely contributes to coexistence mechanisms. Other factors behind diversity maintenance must be examined for large phytoplankton.

Keywords: aggregation; coexistence; individual-based model; phytoplankton; spatial moment equations; spatial point process

*corresponding authors: coralie.picoche@u-bordeaux.fr &

frederic.barraquand@u-bordeaux.fr

26 **Introduction**

27 Phytoplankton communities are among the most important photosynthetic groups on Earth,
28 being at the bottom of the marine food chain, and responsible for approximately half the
29 global primary production (Field *et al.*, 1998). Their contribution to ecosystem functions
30 is only matched by their contribution to biodiversity. Indeed, phytoplankton communities
31 are characterized by a surprisingly high number of species. For example, a single sample
32 as small as a few mL can contain up to seventy species (REPHY, 2017; Widdicombe &
33 Harbour, 2021). This observation is usually called the “paradox of the plankton” (Hutchinson,
34 1961), which refers to the conflict between the observed diversity of species competing for
35 similar resources in a seemingly homogeneous environment, and models predicting that only
36 a few species will persist by outcompeting the others (MacArthur & Levins, 1964; Huisman
37 & Weissing, 1999; Schippers *et al.*, 2001). Phytoplankton models for coexistence are now
38 almost as diverse as their model organisms (Record *et al.*, 2014), but they often describe
39 only a handful of species, which does not correspond to the diversity observed in the field.
40 When modeling rich communities (> 10 species), classical answers to the plankton paradox
41 involving temporal fluctuations (e.g., Li & Chesson, 2016; Chesson, 2018) are not sufficient
42 to maintain a realistic diversity. For instance, we found that a phytoplankton community
43 dynamics model with environmental fluctuations and storage effect still requires extra niche
44 differentiation for coexistence, which manifests in stronger intraspecific than interspecific
45 interactions (Picoche & Barraquand, 2019). However, it is not clear that we should resort
46 to hidden niches to explain phytoplankton coexistence, as most models also make hidden
47 simplifying assumptions that could be relaxed. One that we relax here is mean-field dynamics
48 at the microscale. Indeed, field observations have revealed phytoplankton patchiness for more
49 than a century (Bainbridge, 1957; Stocker, 2012), from the macro- to the micro-scale (Leonard
50 *et al.*, 2001; Doubell *et al.*, 2006; Font-Muñoz *et al.*, 2017).

51 Phytoplankton patchiness can at least be partly explained by the hydrodynamics of their
52 environment: the size of these organisms is mostly below the size of the smallest eddy (i.e.,
53 the Kolmogorov scale). In a typical aquatic environment such as the ocean, phytoplankton
54 individuals are embedded in viscous micro-structures (Peters & Marrasé, 2000) while phy-
55 toplankton populations are displaced by a turbulent flow at slightly larger scales (Martin,
56 2003; Prairie *et al.*, 2012). Phytoplankton organisms therefore live in an environment where
57 fluid viscosity dominates at the scale of an individual but turbulent dispersion dominates on
58 length scales characteristic of a small population of those individuals (Estrada *et al.*, 1987;
59 Prairie *et al.*, 2012).

60 This leads us to consider demography in the context of this environmental variation cre-

ated by hydrodynamic processes. Individual-based models provide a convenient depiction of population dynamics and movement at the microscale (Hellweger & Bucci, 2009). In this framework, population growth is a result of individual births and deaths. Aggregation of individuals can emerge from local reproduction coupled with limited dispersal, which can happen in a fluid where turbulence and diffusion are not strong enough to disperse kin aggregates (Young *et al.*, 2001). The resulting local aggregation can then affect the community dynamics at larger spatial scales, even when all competitors are equivalent (i.e., with equal interaction strengths irrespective of species identity). Indeed, the combination of local dispersal after reproduction and local interactions leads to stronger intraspecific interactions than interspecific interactions at the population level (Detto & Muller-Landau, 2016). This mechanism stabilizes the community, as a high intra-to-interspecific interaction strength ratio makes a species control its abundance more than it controls the abundance of other species, which is associated with coexistence in theoretical models (Levine & HilleRisLambers, 2009; Barabás *et al.*, 2017) and often observed in the field at the population level (Adler *et al.*, 2018; Picoche & Barraquand, 2020). Therefore, the microscale spatial distribution of individuals likely affects the interaction structure within a community (Haegeman & Rapaport, 2008), and may sustain diversity.

Existing models of phytoplankton populations near the Kolmogorov scale — between 1 mm and 1 cm in an oceanic environment (Barton *et al.*, 2014) — focus on a single species and the clustering of its individuals (Young *et al.*, 2001; Birch & Young, 2006; Bouderbala *et al.*, 2018; Breier *et al.*, 2018). They share similarities to dynamic point process models (Law *et al.*, 2003; Bolker & Pacala, 1999; Plank & Law, 2015) developed initially with larger organisms in mind. When phytoplankton individual-based models consider multiple types of organisms, they focus for now on how organisms with opposite characteristics (e.g., increase versus decrease in density with turbulence in Borgnino *et al.*, 2019; Arrieta *et al.*, 2020) segregate spatially, or on coexistence for species that have contrasting trait values (e.g., size in Benczik *et al.*, 2006). This is useful as an explanation of how species with marked differences might coexist. The difficulty of the coexistence problem, however, is that we have to explain how closely related species or genera (e.g., within diatoms), many of whom have similar size, buoyancy, chemical composition, etc., manage to coexist within a single trophic level. This requires modelling *similar* species in a spatially realistic environment and objectively quantifying whether they aggregate or segregate in space.

To do so, we build a multispecies version of the Brownian Bug Model (BBM) of Young *et al.* (2001), an individual-based model which includes an advection process mimicking a turbulent fluid flow, passive diffusion of organisms, as well as stochastic birth and death processes. The initial version of this model (Young *et al.*, 2001) coupled limited dispersal and

local reproduction with ocean-like microscale hydrodynamics, and showed spatial clusters of individuals of the same species. The original BBM was limited to a single species and was illustrated with two-dimensional simulations. The model was not strongly quantitative (Picoche *et al.*, 2022) in the sense that parameters were not informed by current knowledge on phytoplankton biology (numbers of cells per liter, diffusion characteristics, etc.). As phytoplankton organisms live in a three-dimensional environment, informing the model with more realistic parameters requires us to shift to three dimensions. We also extend the model to multiple species, and consider two size classes for our phytoplankton communities, which are either made of nanophytoplankton ($3 \mu\text{m}$ diameter, $\approx 10^6$ cells L^{-1}) or microphytoplankton ($50 \mu\text{m}$, $\approx 10^4$ cells L^{-1}). We populate each community with 3 to 10 different species.

The Brownian Bug model (in its original single-species form as in the multispecies version considered here) is related to spatial branching processes. Without advection, it combines a continuous-time, discrete-state model for population growth and a continuous-time, continuous-space Brownian motion for particle diffusion (Birch & Young, 2006). It is further complexified by a turbulent flow in Young *et al.* (2001); Picoche *et al.* (2022) as well as here. In spite of this complexity, it remains possible to derive the dynamics of pair density functions, which quantify the degree of intra- and interspecific clustering of organisms, via correlations between positions of organisms (see next section). Thus we can understand emergent spatial structure in analytic detail and compare these predictions to the results from three-dimensional simulations. Furthermore, because we do not consider direct interactions between organisms, the multispecies spatial point process that represents the stable state of the BBM is a random superposition of spatial point processes for each species (Illian *et al.*, 2008). This enables us to derive, in addition to pair correlation functions, analytical formulas for the species composition in the neighbourhood of an individual, which are more readily ecologically interpreted than pair density or correlation functions.

Model and spatial statistics

Brownian Bug Model

The Brownian Bug Model (BBM) describes the dynamics of individuals in a turbulent and viscous environment, including demographic processes. The model is continuous in space and time. Here we extend the mostly two-dimensional, monospecific version in Young *et al.* (2001), to three dimensions and S species.

Each individual is characterized by its species identity i and its position $\mathbf{x}^T = (x, y, z)$. The population dynamics are modelled by a linear birth-death process with birth rate λ_i

and death rate μ_i . Each individual independently follows a Brownian motion with diffusivity D_i , and is advected by a common stochastic and chaotic flow modelling turbulence. The model applies in the Batchelor regime, which means that the separation $s(t)$ between two individuals k and l grows exponentially with time with stretching parameter γ , i.e. $s(t) = \ln(|\mathbf{x}_k - \mathbf{x}_l|(t)) \propto 3\gamma t$ (Kraichnan, 1974; Young *et al.*, 2001).

Within a given community (the set of all individuals of the S species), all species share the same parameters: λ_i , μ_i and D_i values can change between communities, as we later consider small and large phytoplankton, but are set to common values within a community. On the contrary, γ describes the environment and is not community-specific, i.e., all individuals are displaced by the same turbulent stirring. For numerical simulations, time needs to be discretized (this is required for diffusion and advection modelling). The approximated model advances through time in small steps of duration of τ . During each interval, events unroll as follows:

1. Demography: each individual can either reproduce with probability $p_i = \lambda_i\tau$ (forming a new individual of the same species i at the same position \mathbf{x} as the parent), die with probability $q_i = \mu_i\tau$, or remain unchanged with probability $1 - p_i - q_i$.
2. Diffusion: each individual moves to a new position $\mathbf{x}(t') = \mathbf{x}(t) + \delta\mathbf{x}(t)$, with $t < t' < t + \tau$. The random displacement $\delta\mathbf{x}(t)$ is drawn from a Gaussian distribution $\mathcal{N}(0, \Delta_i^2)$ with $D_i = \Delta_i^2/2\tau$ the diffusivity. This diffusive step separates the initially coincident pairs produced by reproduction in step 1 above.
3. Turbulence: each individual is displaced by a turbulent flow, modelled with the Pierrehumbert map (Pierrehumbert, 1994), adapted to three dimensions following Ngan & Vanneste (2011). Thus given the position at time t' the updated position at time $t + \tau$ is

$$\begin{aligned} x(t + \tau) &= x(t') + \frac{U\tau}{3} \cos(ky(t') + \phi(t)) \\ y(t + \tau) &= y(t') + \frac{U\tau}{3} \cos(kz(t') + \theta(t)) \\ z(t + \tau) &= z(t') + \frac{U\tau}{3} \cos(kx(t + \tau) + \psi(t)). \end{aligned} \quad (1)$$

Above, U is the velocity of the flow, $k = 2\pi/L_s$ is the wavenumber for the flow at the length scale L_s (see below) and $\phi(t)$, $\theta(t)$, $\psi(t)$ are random phases drawn from a uniform distribution between 0 and 2π ; these phases remain constant during the interval between t and $t + \tau$. The shift from continuous to discrete-time turbulence modelling is described in Section S1 in the Supplementary Information. The velocity U is related to γ . As the separation between two points grows exponentially with parameter 3γ due to turbulence, the exponent γ can be estimated as the slope of $1/3 \langle \ln(s(t)) \rangle = f(t)$ in the absence of diffusion and demography (Young *et al.*, 2001; Picoche *et al.*, 2022).

162 Individuals are distributed in a cube of side length L , with periodic boundary conditions.
 163 The cube dimensions are determined to balance computing costs and realistic concentrations
 164 of individuals; they represent the accumulation of a few volumes of scale L_s .

165 Characterization of the spatial distribution

166 Let W be the observation window (in our case, the whole cube, which we never subsample
 167 hereafter). The state of the system at time t can be described as a collection of S populations,
 168 where the population of species i is made of n_i individuals randomly distributed in W ,
 169 with positions $\mathbf{X}_i(t) = [\mathbf{x}_{1,i}(t), \mathbf{x}_{2,i}(t), \dots, \mathbf{x}_{n_i,i}(t)]$. $\mathbf{X}(t) = [\mathbf{X}_1(t), \dots, \mathbf{X}_S(t)]$ arises from
 170 a stochastic and spatial individual-based model changing through time, but can also be
 171 analyzed as a spatial point process at time t . We note that the point distributions remain
 172 the same for all spatial translations $\boldsymbol{\xi}$ (i.e., the point process described by the set $\mathbf{X} =$
 173 $[\mathbf{x}_1, \mathbf{x}_2, \dots, \mathbf{x}_k]$ is the same as $\mathbf{X}_{\boldsymbol{\xi}} = [\mathbf{x}_1 + \boldsymbol{\xi}, \mathbf{x}_2 + \boldsymbol{\xi}, \dots, \mathbf{x}_k + \boldsymbol{\xi}]$): the process is stationary.

174 A useful method to characterize a spatial point process is the use of spatial moments (il-
 175 lustrated in Section S2 of the SI for simple spatial point processes). These can be theoretically
 176 derived and used to check simulations. The spatial moments of a process are, however, merely
 177 statistical indicators which then need to be related to more easily ecologically interpretable
 178 quantities. This is the role of the dominance index, which we present below.

179 Spatial moments

180 The first-order moment is the intensity of the process, or mean concentration of individuals,
 181 whose empirical estimate is $C_i = \frac{\widehat{N_i(W)}}{V(W)}$, where $\widehat{N_i(W)}$ is the empirical number of individuals
 182 of species i in the cube W and $V(W) = L^3$ is the volume of the cube; it does not give any
 183 information regarding the spatial distribution of individuals, and their spatial correlations.

184 The second-order product density, or pair density $G(r, t)$, is the expected density of pairs
 185 of points separated by a distance r (Law *et al.*, 2003). A similar characteristic can be used for
 186 marked spatial point process. In our case, the marks are the species' identities, and we can
 187 define $G_{ij}(r, t)$, so that $G_{ij}(r, t)d\mathbf{x}_A d\mathbf{x}_B$ is the probability of finding an individual of species
 188 i in volume $d\mathbf{x}_A$ and an individual of species j in volume $d\mathbf{x}_B$, with the distance between
 189 the centers of $d\mathbf{x}_A$ and $d\mathbf{x}_B$ equal to r (pages 219 and 325 in Illian *et al.*, 2008). We define
 190 $\boldsymbol{\xi}$ as the vector connecting the center of $d\mathbf{x}_A$ to the center of $d\mathbf{x}_B$, while $r = |\boldsymbol{\xi}|$ is the radial
 191 distance. We show in Picoche *et al.* (2022) that the intraspecific pair density $G_{ii}(r, t)$, in
 192 three dimensions, is a solution of

$$\frac{\partial G_{ii}}{\partial t}(r, t) = \frac{2D_i}{r^2} \frac{\partial}{\partial r} \left(r^2 \frac{\partial G_{ii}}{\partial r} \right) + \frac{\gamma}{r^2} \frac{\partial}{\partial r} \left(r^4 \frac{\partial G_{ii}}{\partial r} \right) + 2(\lambda_i - \mu_i)G_{ii} + 2\lambda_i C_i \delta(\boldsymbol{\xi}). \quad (2)$$

193 The pair correlation function $g_{ij}(r, t)$, or pcf, can be derived from the pair density and is
 194 defined as

$$g_{ij}(r, t) = \frac{G_{ij}(r, t)}{C_i C_j}. \quad (3)$$

195 The pcf is equal to one when the spatial distribution of species i individuals is random relative
 196 to species j individuals. To compute the intraspecific pcf $g_{ii}(r, t)$ at steady state, considering
 197 a population at equilibrium, we integrate Eq. 2 (see Appendices, Eqs. 19-30) with $\lambda_i = \mu_i$
 198 and obtain

$$g_{ii}(r) = 1 + \frac{\lambda_i}{4\pi D_i C_i \ell_{B,i}} \left(\frac{\ell_{B,i}}{r} + \arctan \left(\frac{r}{\ell_{B,i}} \right) - \frac{\pi}{2} \right), \quad (4)$$

199 where $\ell_{B,i} = \sqrt{2D_i/\gamma}$ approximates the Batchelor scale for species i .

200 The system converges rapidly to the solution in Eq. 4 in the presence of advection.
 201 However, when there is no turbulent advection, convergence is much slower, to the point
 202 that an equilibrium assumption requires unrealistically long timeframes (see Section S3 in
 203 the SI). We therefore need a time-dependent formula for the pcf in the absence of advection,
 204 which can be obtained in the case where $\gamma = 0$ using a Green's function (see derivation in
 205 the Appendices, Eqs. 31-37),

$$g_{ii}(r, t) = 1 + \frac{\lambda_i}{4\pi r D_i C_i} \left\{ 1 - \operatorname{erf} \left(\frac{r}{\sqrt{8D_i t}} \right) \right\}. \quad (5)$$

206 The above equations match when $\gamma \rightarrow 0$ and $t \rightarrow +\infty$.

207 As populations of different species do not directly interact, each population is an inde-
 208 pendent realization of a point process, which means that the distribution of all individuals
 209 within the community at time t is a random superposition of stationary point processes and
 210 thus $g_{ij}(r, t) = 1$ if $i \neq j$ (Illian *et al.*, 2008, p. 326, eq. 5.3.13).

211 Related to the pair correlation function is Ripley's K -function $K(r)$. Using its marked
 212 version, $C_j K_{ij}(r)$ is the average number of points of species j surrounding an individual of
 213 species i within a sphere of radius r (Illian *et al.*, 2008), i.e.,

$$\forall r \geq 0, K_{ij}(r) = \frac{1}{C_j} \mathbb{E}_i (N_j(b(o, r) \setminus \{o\})), \quad (6)$$

214 where \mathbb{E}_i is the expectation with respect to individuals of species i and $N_j(b(o, r) \setminus \{o\})$ is
 215 the number of individuals of species j in the sphere of radius r centered on o , not counting
 216 o itself. $K_{ij}(r)$ is related to $g_{ij}(r)$ as

$$g_{ij}(r) = \frac{K'_{ij}(r)}{4\pi r^2}. \quad (7)$$

217 Combining Eq. 7 and, when $U > 0$, Eq. 4, we can show that (see Appendices, Eqs. 38-44)

$$K_{ii}(r) = \frac{4}{3}\pi r^3 + \frac{\lambda_i r^3}{3D_i C_i \ell_{B,i}} \left(\frac{\ell_{B,i}}{r} + \frac{\ell_{B,i}^3 \log\left(\frac{r^2}{\ell_{B,i}^2} + 1\right)}{2r^3} + \arctan\left(\frac{r}{\ell_{B,i}}\right) - \frac{\pi}{2} \right). \quad (8)$$

218 When $U = 0$, we need a time-dependent solution corresponding to our simulation dura-
219 tion, i.e. (see Appendices, Eq. 46-51)

$$K_{ii}(r, t) = \frac{4}{3}\pi r^3 + \frac{\lambda_i r^2}{C_i D_i} \left(\frac{1}{2} - \frac{1}{2} \operatorname{erf}\left(\frac{r}{\sqrt{8D_i t}}\right) \left(1 - \frac{4D_i}{r^2} t \right) - \frac{\sqrt{2D_i t}}{\sqrt{\pi} r} e^{-\frac{r^2}{8D_i t}} \right). \quad (9)$$

220 For random superposition of stationary point processes, $K_{ij}(r, t) = \frac{4}{3}\pi r^3$ if $i \neq j$ (Illian
221 et al., 2008, p. 324, eq. 5.3.5).

222 Dominance index

223 The dominance index (defined in Table S1 in the Supporting Information of Wiegand *et al.*,
224 2007) is the ratio between the number of conspecifics and the number of individuals of all
225 species surrounding a given individual.

226 Let $M_{ij}(r)$ be the average number of individuals of species j within a circle of radius
227 r around an individual of species i , which can also be written with Ripley's K -function
228 as $M_{ij}(r) = C_j K_{ij}(r)$. $M_{ii}(r)$ corresponds to the conspecific neighbourhood and $M_{io}(r) =$
229 $\sum_{j=1, j \neq i}^S M_{ij}(r)$ corresponds to individuals of all other species. We can then define \mathcal{D}_i as

$$\begin{aligned} \mathcal{D}_i(r) &= \frac{M_{ii}(r)}{M_{ii}(r) + M_{io}(r)} \\ &= \frac{C_i K_{ii}(r)}{\sum_{j=1}^S C_j K_{ij}(r)}. \end{aligned} \quad (10)$$

230 When individuals of the same species i tend to cluster, $\mathcal{D}_i(r)$ tends to 1 while it tends to
231 the proportion of individuals of species i in the whole community when the distribution is
232 uniform (Section S2 of the SI).

233 Using Eq. 9 and 10, we obtain the formula for the dominance index in the presence of
234 advection as

$$\mathcal{D}_i(r) = \frac{\frac{\lambda_i}{3D_i \ell_{B,i}} \left(\frac{\ell_{B,i}}{r} + \frac{\ell_{B,i}^3 \log\left(\frac{r^2}{\ell_{B,i}^2} + 1\right)}{2r^3} + \arctan\left(\frac{r}{\ell_{B,i}}\right) - \frac{\pi}{2} \right) + \frac{4}{3}\pi C_i}{\frac{\lambda_i}{3D_i \ell_{B,i}} \left(\frac{\ell_{B,i}}{r} + \frac{\ell_{B,i}^3 \log\left(\frac{r^2}{\ell_{B,i}^2} + 1\right)}{2r^3} + \arctan\left(\frac{r}{\ell_{B,i}}\right) - \frac{\pi}{2} \right) + \sum_{j=1}^S \frac{4}{3}\pi C_j}. \quad (11)$$

235 In the absence of advection ($U = 0, \gamma = 0$), we use the time-dependent dominance index,
236 computed similarly:

$$\mathcal{D}_i(r, t) = \frac{\frac{\lambda_i}{D_i r} \left(\frac{1}{2} - \frac{1}{2} \operatorname{erf} \left(\frac{r}{\sqrt{8D_i t}} \right) \left(1 - \frac{4D_i}{r^2} t \right) - \frac{\sqrt{2D_i t}}{\sqrt{\pi} r} e^{-\frac{r^2}{8D_i t}} \right) + \frac{4}{3}\pi C_i}{\frac{\lambda_i}{D_i r} \left(\frac{1}{2} - \frac{1}{2} \operatorname{erf} \left(\frac{r}{\sqrt{8D_i t}} \right) \left(1 - \frac{4D_i}{r^2} t \right) - \frac{\sqrt{2D_i t}}{\sqrt{\pi} r} e^{-\frac{r^2}{8D_i t}} \right) + \sum_{j=1}^S \frac{4}{3}\pi C_j}. \quad (12)$$

237 Parameters

238 We model two types of organisms: microphytoplankton (defined by a diameter between 20
239 and 200 μm , here 50 μm) and nanophytoplankton (defined by a diameter between 2 and 20
240 μm , here 3 μm). These two groups are characterized respectively by a low diffusivity, slow
241 growth and lower concentration vs. high diffusivity, fast growth and higher concentration.
242 Organisms are displaced by a turbulent fluid whose velocity defines the time scale of the
243 discretized model: we give here the reasoning behind parameter values, keeping in mind that
244 our model parameters are only approximate. Main parameter definitions and values are given
245 in Table 1.

246 Advection

247 We first consider the advection process, due to the turbulence of the environment. We
248 only consider the Batchelor-Kolmogorov regime, i.e., the size of the volume W is below the
249 size of the smallest eddy, but above the smallest length scale of fluctuations in nutrient
250 concentrations. The defining scale of the environment therefore corresponds to a Reynolds
251 number

$$\operatorname{Re} = \frac{U}{k\nu} \approx 1 \quad (13)$$

252 where $\nu = 10^{-6} \text{ m}^2 \text{ s}^{-1}$ is the kinematic viscosity for water. The smallest wavenumber k
253 corresponds to the largest length scale L_s (Kolmogorov scale), i.e., $k = 2\pi/L_s$, with $L_s \approx 1$
254 cm in the ocean (Barton *et al.*, 2014). The definition of the Reynolds number leads to

$$\begin{aligned} 1 &\approx \frac{UL_s}{2\pi\nu} \\ \Leftrightarrow U &\approx \frac{2\pi\nu}{L_s}. \end{aligned} \quad (14)$$

255 This means that $U = 6.3 \times 10^{-4} \text{ m s}^{-1} = 5.4 \times 10^3 \text{ cm d}^{-1}$. Using $U\tau/3 = 0.5 \text{ cm}$ as in
256 Young *et al.* (2001), we have $\tau = 2.8 \times 10^{-4} \text{ d} = 24 \text{ s}$. When $U\tau/3 = 0$, the environment is
257 only diffusive, we keep the same value for τ . For $U\tau/3 = 0.5 \text{ cm}$, $\gamma = 1231 \text{ d}^{-1}$.

258 **Diffusion**

259 If we use the Stokes-Einstein equations (Einstein, 1905, cited from Dusenbery, 2009), diffu-
260 sivity can be computed with

$$D_i = \frac{RT}{N_A} \frac{1}{6\pi\eta a_i} \quad (15)$$

261 where $R = 8.314 \text{ J K}^{-1} \text{ mol}^{-1}$ is the molar gas constant, $T = 293 \text{ K}$ is the temperature,
262 $N_A = 6.0225 \times 10^{23}$ is Avogadro's number, $\eta = 10^{-3} \text{ m}^{-1} \text{ kg s}^{-1}$ is the dynamic viscosity of
263 water and a_i is the radius of the organism considered.

264 Using $D_i = \frac{\Delta_i^2}{2\tau}$, we find that

$$\begin{aligned} \Delta_i &= \sqrt{2\tau D_i} \\ \Leftrightarrow \Delta_i &= \sqrt{\frac{RT}{N_A} \frac{\tau}{3\pi\eta a_i}}. \end{aligned} \quad (16)$$

265 We consider $a_n = 1.5 \mu\text{m}$ for nanophytoplankton individuals and $a_m = 25 \mu\text{m}$ for micro-
266 phytoplankton individuals, which allows us to compute Δ_n and Δ_m (see Table 1).

267 **Ecological processes**

268 We study the community at equilibrium, with the birth rate equal to the death rate, i.e.,
269 $p_i = q_i \forall i$. We use a microphytoplankton doubling rate of 1 d^{-1} (Bissinger *et al.*, 2008) and
270 consider the fastest-growing nanophytoplankton species, corresponding to a diameter of $3 \mu\text{m}$
271 (Bec *et al.*, 2008), for which the doubling rate is between 2 and 3 d^{-1} (set to 2.5 d^{-1}
272 here).

Parameter	Definition	Value
p_m, q_m	Probability of reproducing/dying for microphytoplankton individuals	2.8×10^{-4}
p_n, q_n	Probability of reproducing/dying for nanophytoplankton individuals	6.9×10^{-4}
U	Turbulent advection speed	$\{0, 0.06\} \text{ cm.s}^{-1}$
Δ_m	Diffusion parameter for microphytoplankton individuals	$6.4 \times 10^{-5} \text{ cm}$
Δ_n	Diffusion parameter for nanophytoplankton individuals	$2.6 \times 10^{-4} \text{ cm}$

Table 1: Definitions and values of the main parameters used in the three-dimensional BBM, assuming the duration of a time step τ is 24 seconds.

273 **Range of interaction**

274 As we examine individual aggregation and its potential effects on interactions between species,
275 we have to ascertain the volume in which an individual can be affected by the presence of
276 other individuals, or affect other individuals. We only consider here interactions due to
277 competition for nutrients, and therefore need to define a nutrient depletion volume. We

278 approximate this volume as the sphere of radius r where $C(r) \leq 90\%C_\infty$ with C_∞ the
 279 background concentration of the nutrient. The radius of this nutrient depletion volume is
 280 maximized when the individual is in stagnant water so that diffusion is the only hydrodynamic
 281 process. In this case, the depletion radius corresponds to 10 times the radius of the individual
 282 (Jumars *et al.*, 1993; Karp-Boss *et al.*, 1996). We define the maximum distance which allows
 283 for potential interactions (due to competition for resources) between two individuals of radius
 284 a_i and a_j as $d_{\text{threshold}}$, and the corresponding volume of potential interactions around an
 285 organism as $V_{\text{int}} = 4/3\pi d_{\text{threshold}}^3$ with

$$d_{\text{threshold}} = 10a_i + 10a_j. \quad (17)$$

286 We consider this maximum value as our baseline, keeping in mind that turbulence reduces
 287 the size of the nutrient depletion volume and increases the nutrient flux to the cell (Arnott
 288 *et al.*, 2021). We caution that determination of the shape of the nutrient depletion volume
 289 in the presence of turbulence is too complex to be addressed here (Karp-Boss *et al.*, 1996).

290 We consider a total volume of 1000 cm^3 for microphytoplankton and 10 cm^3 for nanophy-
 291 toplankton (volumes are adapted to balance realistic concentrations and computation time)
 292 with periodic boundary conditions. Individuals are uniformly distributed in the cube at
 293 the beginning of the simulation. We run an idealized simulation with 3 species with an
 294 even abundance distribution of about $10^4 \text{ cells L}^{-1}$ for microphytoplankton (Picoche & Bar-
 295 raquand, 2020) and $10^6 \text{ cells L}^{-1}$ for nanophytoplankton individuals (Edwards, 2019). We
 296 then model a more realistic community with 10 species having a skewed abundance distri-
 297 bution (between 55,000 and 400 cells L^{-1} for microphytoplankton, according to observations
 298 of field abundance distributions in Picoche & Barraquand, 2020, and multiplied by 10^2 for
 299 nanophytoplankton). All simulations are run for 1000 time steps of duration τ (correspond-
 300 ing to approximately 6h40). The computation of g and K of simulated distributions is
 301 explained in Section S4 of the SI. The code for all simulations and analyses can be found at
 302 https://github.com/CoraliePicoche/brownian_bug_3D/.

303 Results

304 We show an example of nanophytoplankton spatial distributions with and without advection
 305 at the end of a simulation in Fig. 1: clustering is not visible to the naked eye, even when
 306 zooming in on the observation volume, in the presence of advection, but removing turbulence
 307 helps visualising small aggregates of conspecifics. Microphytoplankton distributions are not
 308 so easy to analyse as no clusters can be detected from visual observations (although it may

³⁰⁹ actually be present), whether advection is included or not (Section S5 of the SI). Statistics
³¹⁰ are therefore needed to go further in detecting patterns of aggregation.

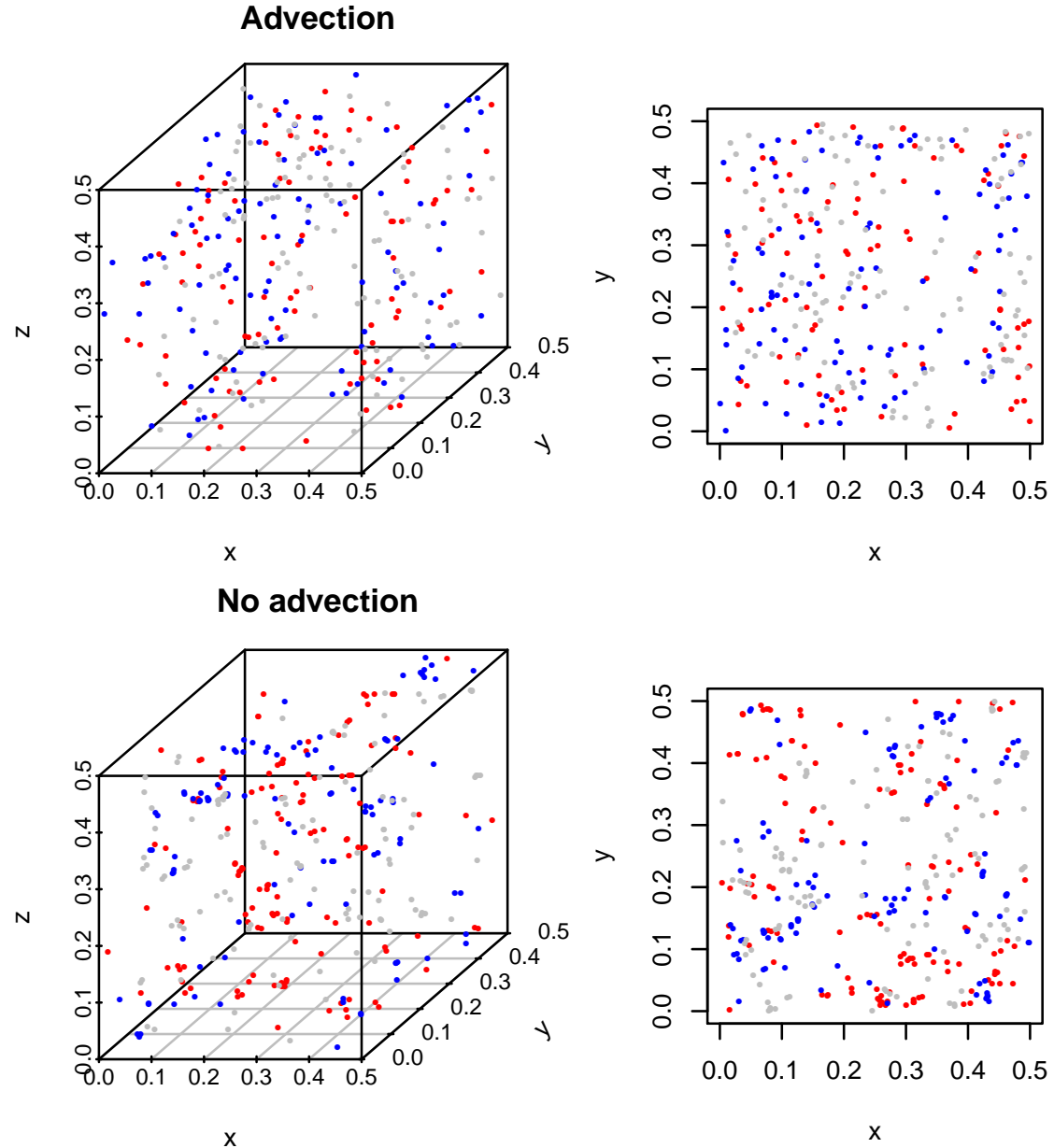


Figure 1: Spatial distributions of a 3-species community of nanophytoplankton with and without advection with density $C = 10^3$ cells cm^{-3} after 1000 time steps. Each color corresponds to a different species. On the left-hand side, only a zoom on a $0.5 \times 0.5 \times 0.5 \text{ cm}^3$ cube is shown, and its projection on the x-y plane is shown on the right-hand side.

³¹¹ Ripley's K -functions extracted from numerical simulations match theoretical formula
³¹² (Fig. 2) for both types of organisms, which also indicates that dominance indices extracted
³¹³ from the simulations match theoretical expectations.

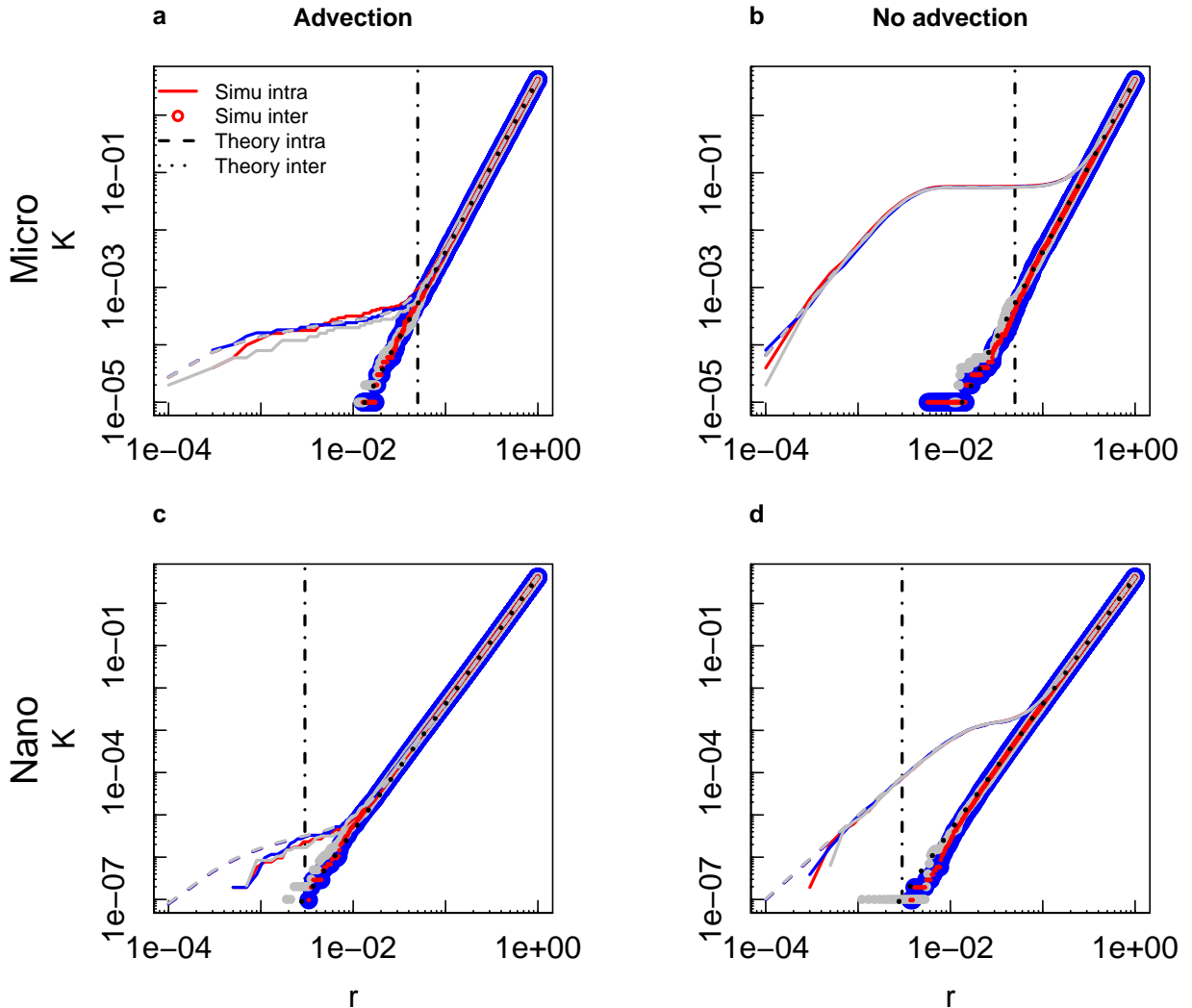


Figure 2: Comparison of theoretical and simulated Ripley's K -functions as a function of distance (in cm) for microphytoplankton (a-b) and nanophytoplankton (c-d) in a 3-species community with even abundance distributions after 1000 timesteps, with (a, c) and without (b, d) advection. Each color represents a different species. Intraspecific K -functions are shown with dashed (theoretical values) and solid (simulated values) lines. Interspecific K -functions are shown with dotted lines (theoretical values) and circles (simulated values). The black dash-dotted line corresponds to the threshold considered as the maximum distance for nutrient-based competition.

³¹⁴ Dominance indices all follow a similar pattern (Fig. 3 and 4). The dominance index is
³¹⁵ close to 1 for small distances: there is always a scale at which an organism is surrounded
³¹⁶ almost only by conspecifics. The index then decreases sharply to converge at large distances
³¹⁷ (close to 1 cm) to the proportion of the focus species in the whole community, as it would for
³¹⁸ a uniform spatial distribution. Patterns differ at intermediate ranges of distances between

319 organisms.

320 In the presence of advection, the dominance index starts decreasing for a distance be-
321 tween 5 and 10 times smaller than when advection is absent, which indicates that organisms
322 are closer to heterospecifics when their environment is turbulent. A quasi-uniform distribu-
323 tion is also reached for smaller distances with advection than without. Microphytoplankton
324 species start mixing for distances larger than for nanophytoplankton species irrespective of
325 the hydrodynamic regime surrounding them.

326 In a 3-species community with the same initial abundances, in the presence of advection,
327 microphytoplankton dominance indices are between 0.37 and 0.47 at the distance thresh-
328 old for potential interactions, while they are between 0.80 and 0.94 for nanophytoplankton
329 species. In the absence of turbulence, dominance indices are all above 0.98 when the distance
330 threshold is reached (Fig. 3). Microphytoplankton organisms are therefore as likely to share
331 their depletion volume with conspecifics as they are with heterospecifics, but only when tur-
332 bulent advection is accounted for, whereas nanophytoplankton organisms always have almost
333 only conspecifics around them.

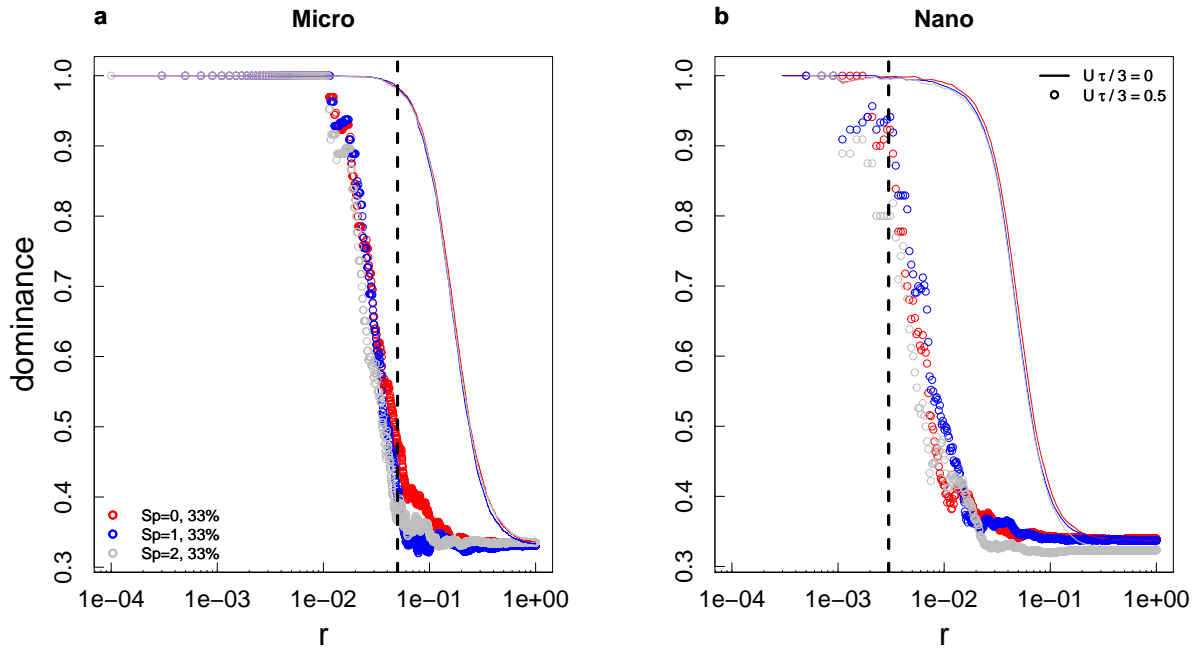


Figure 3: Dominance indices as a function of distance (in cm) for microphytoplankton (a) and nanophytoplankton (b) in a 3-species community with even abundance distributions (final proportions in the community are indicated in the figure) after 1000 timesteps, with (circles) and without (lines) advection. Each color represents a different species. The black dashed line corresponds to the threshold considered as the maximum distance for nutrient-based competition.

More mixing in microphytoplankton than nanophytoplankton, and more mixing with advection, also holds when considering a 10 species-community with a skewed abundance distribution (Fig. 4), but dominance indices are overall lower in communities with more species and with less even abundances. In the presence of advection, microphytoplankton dominance indices at the distance threshold are between 0.34 (for the most abundant species) and 0.033 (for one of the least abundant species), while they are between 0.90 and 0.85 when advection is not taken into account. Nanophytoplankton species, too, are more mixed than in the 3 species-community: dominance indices vary between 0.54 and 0.2 when the depletion threshold is reached (with an exception of 0 for one particular species which had no conspecific for distances below 10^{-2} cm) when organisms are displaced by turbulence, while the same quantity is between 1 and 0.97 when they are only subject to diffusion.

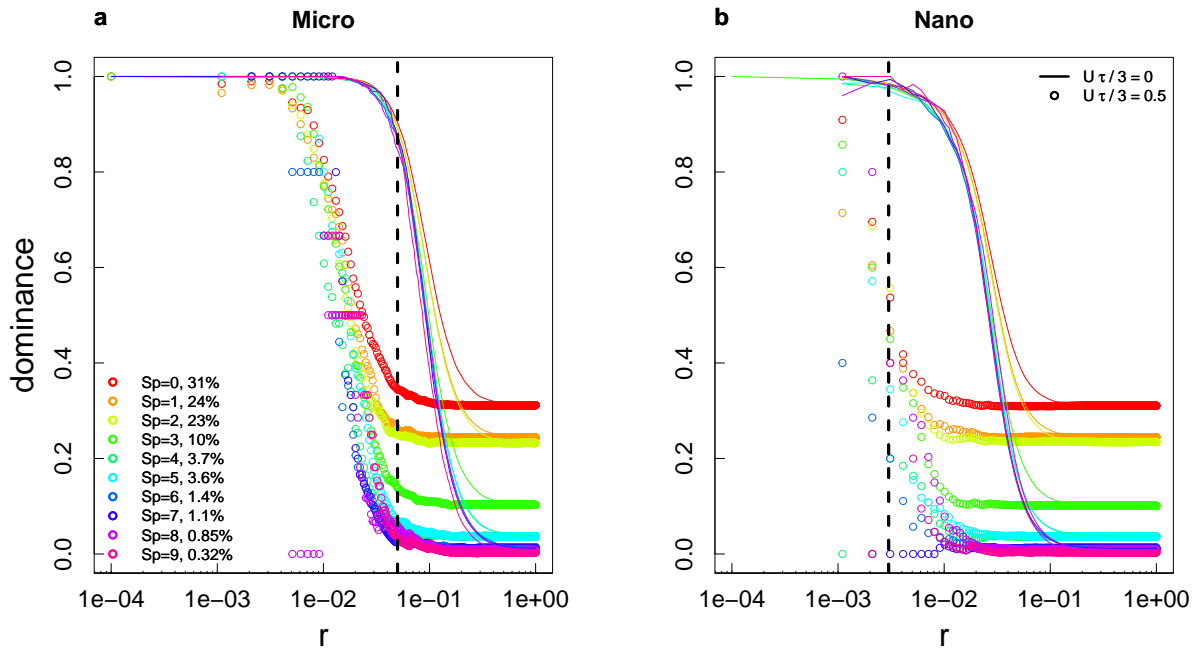


Figure 4: Dominance indices as a function of distance (in cm) for microphytoplankton (a) and nanophytoplankton (b) in a 10-species community with a skewed abundance distribution (final proportions in the community are indicated in the figure) after 1000 timesteps, with (circles) and without (lines) advection. Each color represents a different species. The black dashed line corresponds to the threshold considered as the maximum distance for nutrient-based competition.

Differences in spatial distributions are not only due to organism sizes, which determine their demographic and hydrodynamic properties, but also to their abundances (here set through initial values). In the presence of turbulence, the threshold distance at which dominance falls below 95% is smaller for more abundant species (Fig. 5 a-b). Abundant species

tend to be present nearly everywhere when they are mixed in the environment. Therefore,
 they are also more likely to be close to a heterospecific, but still have more conspecifics close
 to them than the less abundant species ($\mathcal{D}(d_{\text{threshold}})$ increases with abundance, Fig. 5 c-d).
 However, this increase is less marked for nanophytoplankton than for microphytoplankton
 (Fig. 5 c-d). When turbulence is absent, the relationships with abundance are unclear,
 possibly affected by sampling effects, and we refrain from interpreting them.

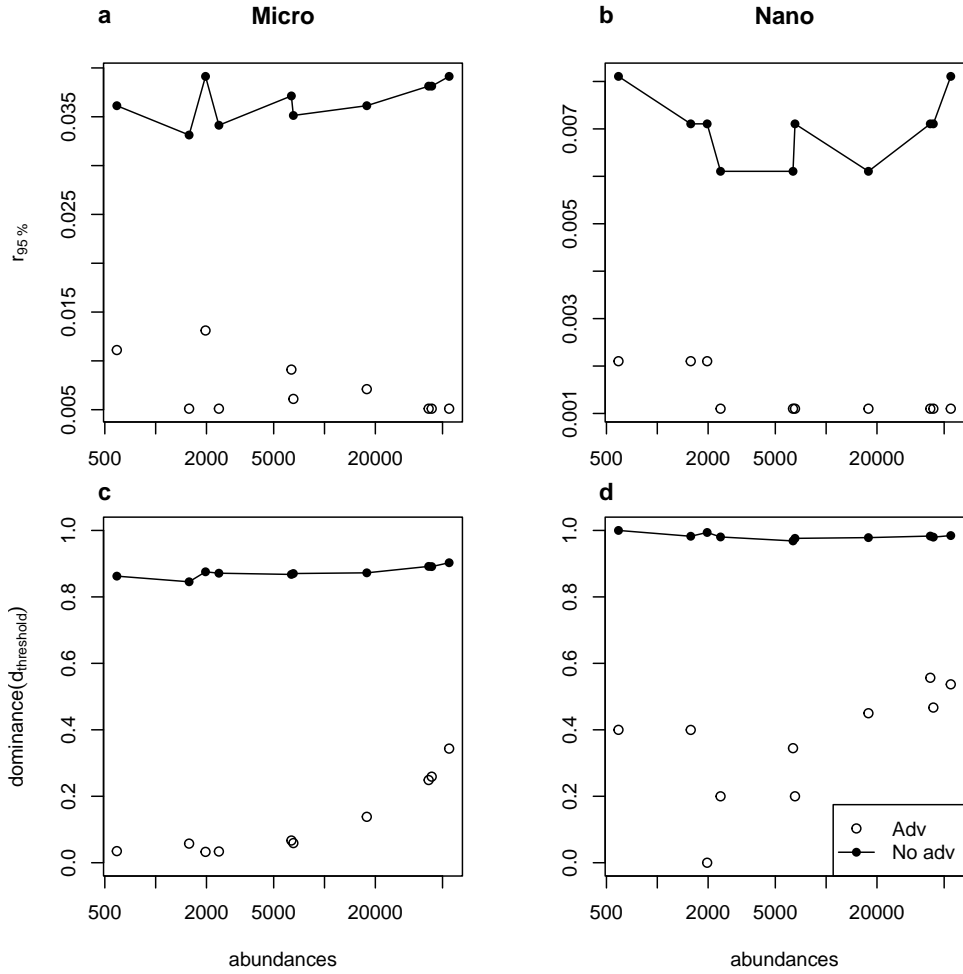


Figure 5: Minimum distances (in cm) between points for dominance to drop below 95% (a and b) and dominance at a distance corresponding to the threshold for competition (c and d) as a function of abundances (note the logarithmic scale on the x-axis) for microphytoplankton and nanophytoplankton. We consider cases with and without advection in a 10-species community with a skewed abundance distribution.

355 **Discussion**

356 We designed a stochastic, three-dimensional, individual-based model of the spatial distri-
357 bution of multiple species in a viscous and turbulent flow. We conducted both mathemat-
358 ical analyses and numerical simulations to quantify spatial correlations in the distribution
359 of organisms. We focused on the pair correlation function and Ripley's K -function, for
360 which numerical and theoretical analyses showed a good agreement, and extracted a more
361 ecologically-oriented metric from them, i.e., the dominance index. This statistic is the *local*
362 average ratio of conspecifics, i.e., the number of organisms of the focal species in the neigh-
363 bourhood of an individual of the same species, divided by the total number of organisms in
364 that neighbourhood. Intraspecific clustering corresponds to a dominance index close to 1,
365 which decreases when interspecific mixing increases. The choice of this index was motivated
366 by two reasons: (1) it is at its core a proportion of a focus species in a certain volume, i.e.
367 a scale-dependent, localized metric bounded between 0 and 1 as opposed to other statistics
368 whose values are less directly interpreted, and (2) it is easy to relate to coexistence theory
369 as it describes the environment of an organism in terms of heterospecifics and conspecifics,
370 which can, under certain hypotheses that we discuss below, be related to interspecific and
371 intraspecific interactions. Comparing the distributions of organisms of different sizes, we
372 showed that the presence of turbulence always increased mixing (results are robust to slight
373 modifications in the computation of advection velocity U , shown in Section S7 of the SI).
374 The species composition around an organism depended on its size, which mechanically deter-
375 mines its hydrodynamic properties (diffusivity), and is linked with its ecological characteris-
376 tics (growth rate and density). Microphytoplankters (20 to 200 μm), larger cells with lower
377 diffusivity, growth rate and abundance, were on average further away from other cells, due
378 to their lower concentrations (Figure S10 of the SI), than nanophytoplankters (2 to 20 μm).
379 However, they were surrounded by more heterospecifics than conspecifics within a volume of
380 potential interactions, whose radius is defined as the maximum distance for which nutrient
381 depletion volumes of two different individuals may overlap. If we consider that interactions
382 between species (not modelled directly here because of timescale issues, see below) could
383 occur with equal probability at all distances within the volume of potential interactions, we
384 would conclude that microphytoplankters are more likely to interact with individuals from
385 other species than with individuals of their own species. This affirmation is, however, condi-
386 tional upon interactions at 10 cell diameters from an individual being equally likely than at 1
387 diameter from an individual. If we keep in mind that interactions are more likely or stronger
388 at very short distances, microphytoplankters may still experience more frequent effects of
389 conspecifics than heterospecifics.

To see this, let us first focus on the smallest distances between organisms. The nearest neighbour of an organism was always an organism of the same species, and the minimum distance between conspecifics was always lower than expected for a uniform distribution (Section S6 of the SI). The dominance index remained close to 1 for distances below 10^{-2} cm or 10^{-3} cm for microphytoplankton and nanophytoplankton respectively. There was therefore always *some* intraspecific aggregation, i.e. conspecifics were always closer than heterospecifics at the smallest distances. This is due to the prevalence of demographic processes at individual scales, because an individual acts as a source point for other organisms of the same species, and hydrodynamic processes do not separate conspecifics fast enough to prevent aggregation. If we consider that interaction strengths are a smoothly decaying function of distance, a common assumption in spatial coexistence models (e.g., Bolker & Pacala, 1999; Law *et al.*, 2003), this implies that population-level intraspecific interactions could be stronger than interspecific interactions due to intraspecific micro-scale aggregation. However, the mechanisms of competition at this scale are poorly known, likely relying on multiple types of resources with different distributions in the environment, effects on the cell, uptakes, etc. Rather than weighting much more heavily the potential interactions with the closest neighbour(s) through an interaction kernel, we therefore chose conservatively to define a maximum distance for two organisms to possibly affect the concentrations of elements in the environment of each other. We consider that, at all distances below this threshold, interactions could happen between organisms. We continue the discussion with that simplification in mind, and explicitly mention when it is relaxed.

Dominance indices began to decrease at distances above 10^{-3} cm, still below the maximum distance for interactions. At this distance and above, the balance between heterospecifics and conspecifics was much more sensitive to different phytoplankters' demographic and hydrodynamic traits. The species composition of an organism's neighbourhood depended on its size: nanophytoplankton organisms mainly shared their volume of potential interactions with conspecifics (the dominance index remained close to 1, even near the distance threshold, i.e. the maximum distance for the overlap of nutrient depletion volumes) while microphytoplankton organisms could affect both conspecifics and heterospecifics (the dominance index was often below 0.5 at the distance threshold, i.e. an individual's depletion zone probably overlapped with more heterospecifics' than conspecifics'). Microphytoplankters were therefore more likely to share their depletion volume with heterospecifics than nanophytoplankters. The rate of production of new microphytoplankton conspecifics was not sufficient to compensate for the mixing induced by turbulence and diffusivity, even though the diffusivity of microphytoplankters was smaller than that of nanophytoplankters. There may therefore be different mechanisms at play at the community level for microphytoplankton and nanophyto-

426 plankton to maintain coexistence. For nanophytoplankton, the spatial structure likely leads
427 to more interactions between conspecifics than between heterospecifics. The spatial distribu-
428 tion of microphytoplankton species, on the contrary, encourages more interactions between
429 heterospecifics. If we consider that local interaction strengths are equal within the volume
430 of potential interactions, scaling to the population level, we would likely observe stronger
431 intra- over interspecific interactions for nanophytoplankton (a key factor in coexistence the-
432 ory, Barabás *et al.*, 2017) but not necessarily so for microphytoplankton. Using a timescale
433 separation argument, we show in Section S8 in the SI how stronger interactions at popula-
434 tion level than individual level may arise in a Lotka-Volterra model whose spatial structure is
435 summed up by the dominance indices evidenced here. Stronger intra- than interspecific com-
436 petition may arise at population level even when assuming that all local interaction strengths
437 between individuals are equal, regardless of the identity of competitors.

438 All of the above discussion is based on a microphytoplankter's neighbourhood in its nutri-
439 ent depletion volume. To simplify the computation, we used maximum volumes of potential
440 interactions, corresponding to a diffusive-only flow of nutrient particles. But when fluid tur-
441 bulence increases, nutrient uptake increases, and the size of the depletion zone decreases
442 (Karp-Boss *et al.*, 1996). The proportion of change in the depletion volume increases with
443 the size of organisms: a 10 μm -diameter organism might not experience any change, while
444 the uptake of a 100 μm -diameter organism would increase by at least 50% (Karp-Boss *et al.*,
445 1996). Therefore the volume of potential interactions shrinks in the presence of turbulence
446 for microphytoplankton, but not necessarily for nanophytoplankton. This could be one addi-
447 tional reason why microphytoplankters might still be surrounded by conspecifics at ecologically
448 meaningful distances and interacting more frequently with them.

449 Up to now, we have only focused on the dominance index, a localized proportion of
450 conspecifics. However, interactions also depend on the absolute densities of individuals. Me-
451 chanically, when density decreases, the distances between neighbours increase, which explains
452 that the distances between the low-abundance microphytoplankters tended to be greater than
453 distances between the more abundant nanophytoplankters (Section S6 of the SI). Explicit
454 mathematical models using pair densities to express interaction rates (e.g. Law *et al.*, 2003;
455 Plank & Law, 2015) may be able to incorporate those effects; however, as we highlight be-
456 low, the timescales and spatial correlations that are seen in such models may not necessarily
457 represent faithfully phytoplankton community dynamics.

458 Contrary to other similar models (e.g., Birch & Young, 2006; Bouderbala *et al.*, 2018),
459 we did not consider explicit effects of local density on survival and fertility rates. Outside of
460 simply maintaining analytical tractability, we had another, more biological reason to do so:
461 we cannot be sure that these local density-dependencies make sense in our phytoplankton

462 context. To understand why, consider that even if a species abundance is locally tripled,
463 competition might not directly ensue at the time scales covered by our model (≈ 7 h),
464 if nutrient depletion has not had time to set in yet. Even if we considered longer time
465 frames, we would need lagged local density-dependencies, which are to our knowledge not
466 leading to tractable spatial branching or dynamic point processes. We could, of course,
467 directly model nutrients, perhaps as resource “points” with a dynamics of their own (Murrell,
468 2005; North & Ovaskainen, 2007), which in turn change the reproduction or death rate
469 of individuals. If the resource points risk being depleted, this entails a negative spatial
470 correlation between organisms and their resources (Murrell, 2005; Barraquand & Murrell,
471 2012). And that is where such models might be inadequate. The phycosphere, a micro-
472 environment at the periphery of a phytoplankton organism where communities of bacteria
473 interact (Seymour *et al.*, 2017), can also impact phytoplankton fitness, both positively (cross-
474 feeding) and negatively (algalicidal activities of bacteria). This can sometimes lead to an
475 accumulation of key resources close to the phytoplankton. This will lead to positive spatial
476 correlations between consumers and their resources, and we currently do not have theoretical
477 models to represent this process (short of modelling precisely the spatial distribution of these
478 bacteria).

479 Our model should be viewed as a first model of spatial distributions of multiple phyto-
480 plankton species in a realistic, three-dimensional environment at the microscale, describing
481 only basic hydrodynamic and demographic processes. Using this model, we were able to
482 predict whether phytoplankters could be in contact with individuals of their own or other
483 species, and emit reasonable conjectures regarding potential intra vs interspecific interac-
484 tions between species, emerging at the population level through spatial distributions (Detto
485 & Muller-Landau, 2016). It is worthwhile to keep in mind that there are many remaining
486 features of phytoplankton physiology and life histories which we do not address here, but
487 which may affect spatial distributions. Many phytoplankters are able to move actively in
488 three dimensions, which can favour cluster formation (Breier *et al.*, 2018). Even those who
489 are believed to move passively actually often move along the vertical dimension by regulat-
490 ing their buoyancy (Reynolds, 2006), and can at times aggregate to form pairs (Font-Muñoz
491 *et al.*, 2019). Finally, a part of spatial structure is explained by the partially colonial nature
492 of microphytoplankton (Kiørboe *et al.*, 1990). This clearly calls for viewing our model as
493 a null model to which more complex mechanistic models and their spatial outputs can be
494 compared.

495 **Acknowledgments**

496 FB and CP were supported by the grant ANR-20-CE45-0004. CP was supported by a PhD
497 grant from the French Ministry of Research.

498 **Appendices**

499 **Derivation of the spatial characteristics of the Brownian Bug Model**

500 We show here how to compute the monospecific pair correlation function and Ripley's K -
501 function of the Brownian Bug Model (see Young *et al.*, 2001 and Picoche *et al.*, 2022 for
502 a detailed derivation of the master equation). As these formula only apply to intraspecies
503 pairs, we ignore species' index in the following for the sake of clarity. Similar formula for
504 well-known spatial point processes are given in the Supplementary Information, for readers
505 who want to understand better the properties of these spatial statistics.

506 **Proof of Eq. 4 and Eq. 5**

507 In three dimensions, when the birth rate λ is the same as the mortality rate μ , the pair
508 density $G(r)$ is a solution of

$$\frac{\partial G}{\partial t} = \frac{2D}{r^2} \frac{\partial}{\partial r} \left(r^2 \frac{\partial G}{\partial r} \right) + \frac{\gamma}{r^2} \frac{\partial}{\partial r} \left(r^4 \frac{\partial G}{\partial r} \right) + 2\lambda C \delta(\xi). \quad (18)$$

Steady-state solution We first compute the steady-state solution, *i.e.*

$$\begin{aligned} 0 &= \frac{2D}{r^2} \frac{\partial}{\partial r} \left(r^2 \frac{\partial G}{\partial r} \right) + \frac{\gamma}{r^2} \frac{\partial}{\partial r} \left(r^4 \frac{\partial G}{\partial r} \right) + 2\lambda C \delta(\xi) \\ 0 &= 4\pi r^2 \left(\frac{2D}{r^2} \frac{\partial}{\partial r} \left(r^2 \frac{\partial G}{\partial r} \right) + \frac{\gamma}{r^2} \frac{\partial}{\partial r} \left(r^4 \frac{\partial G}{\partial r} \right) + 2\lambda C \delta(\xi) \right) \\ 0 &= 4\pi \left(2D \frac{\partial}{\partial r} \left(r^2 \frac{\partial G}{\partial r} \right) + \gamma \frac{\partial}{\partial r} \left(r^4 \frac{\partial G}{\partial r} \right) \right) + 4\pi r^2 2\lambda C \delta(\xi). \end{aligned} \quad (19)$$

We can then integrate Eq. 18 over a small sphere centered on an individual, with radius ρ . Let us first note that

$$\begin{aligned} & \int_{\mathbb{R}^3} \delta(\boldsymbol{\xi}) d\boldsymbol{\xi} = 1 \\ \Leftrightarrow & \int_0^{2\pi} \int_0^\pi \int_0^\rho \delta(r) \delta(\phi) \delta(\theta) r^2 \sin(\phi) dr d\phi d\theta = 1 \\ \Leftrightarrow & 4\pi \int_0^\rho \delta(r) r^2 dr = 1. \end{aligned} \quad (20)$$

Using Eq. 19 and 20,

$$\begin{aligned} 0 &= 4\pi \left(2Dr^2 \frac{\partial G}{\partial r} + \gamma r^4 \frac{\partial G}{\partial r} \right) + 2\lambda C \\ \Leftrightarrow & \frac{\partial G}{\partial r} = -\frac{1}{4\pi} \frac{2\lambda C}{2Dr^2 + \gamma r^4}. \end{aligned} \quad (21)$$

We can integrate Eq. 21 between ρ and ∞ . As $G(\infty) = C^2$,

$$C^2 - G(\rho) = -\frac{\lambda C}{2\pi} \int_\rho^\infty \frac{1}{2Dr^2 + \gamma r^4} dr. \quad (22)$$

We first compute the primitive $A = \int \frac{1}{2Dr^2 + \gamma r^4} dr$.

$$A = \int \frac{1}{r^2 (2D + \gamma r^2)} dr \quad (23)$$

$$= \int \frac{1}{2Dr^2} - \frac{\gamma}{2D(2D + \gamma r^2)} dr \quad (24)$$

$$= -\frac{1}{2Dr} - \frac{\gamma}{2D} \int \frac{1}{2D \left(1 + \left(\sqrt{\frac{\gamma}{2D}} r \right)^2 \right)} dr. \quad (25)$$

⁵⁰⁹ With a change of variable $u = \sqrt{\frac{\gamma}{2D}} r$, using $\int \frac{1}{1+u^2} = \arctan(u)$, we have

$$A = -\frac{1}{2Dr} - \frac{\sqrt{\gamma} \arctan \left(\frac{\sqrt{\gamma}r}{\sqrt{2D}} \right)}{2\sqrt{2D}\sqrt{D}} + K \quad (26)$$

⁵¹⁰ where K is a constant. We can now compute $B = [A]_\rho^\infty$.

$$B = -\frac{\sqrt{\gamma}\pi}{4\sqrt{2D}\sqrt{D}} + \frac{1}{2D\rho} + \frac{\sqrt{\gamma} \arctan \left(\frac{\sqrt{\gamma}\rho}{\sqrt{2D}} \right)}{2\sqrt{2D}\sqrt{D}}. \quad (27)$$

This leads to

$$G(\rho) = C^2 + \frac{\lambda C}{2\pi} B \quad (28)$$

$$= C^2 + \frac{\lambda C}{2\pi} \left[\frac{1}{2D\rho} + \frac{\sqrt{\gamma} \arctan\left(\frac{\sqrt{\gamma}\rho}{\sqrt{2D}}\right)}{2\sqrt{2D}\sqrt{D}} - \frac{\sqrt{\gamma}\pi}{4\sqrt{2D}\sqrt{D}} \right]. \quad (29)$$

Finally, the pair correlation function $g = G/C^2$ is defined as

$$g(\rho) = \frac{\lambda}{4\pi CD} \left(\frac{\sqrt{\gamma} \arctan\left(\frac{\sqrt{\gamma}\rho}{\sqrt{2D}}\right)}{\sqrt{2D}} + \frac{1}{\rho} - \frac{\pi\sqrt{\gamma}}{2\sqrt{2D}} \right) + 1. \quad (30)$$

Time-dependent solution In the absence of advection by turbulent diffusion ($U = 0, \gamma = 0$), convergence to the steady-state solution can be very slow (more than a week, see Section S3 in the SI). In order to keep a realistic timeframe, we need to compute a time-dependent solution. We can get back to Eq. 18 with $\gamma = 0$, which yields

$$\frac{\partial G}{\partial t} = \frac{2D}{r^2} \frac{\partial}{\partial r} \left(r^2 \frac{\partial G}{\partial r} \right) + 2\lambda C \delta(\xi). \quad (31)$$

Assuming an isotropic environment, this means

$$\frac{\partial G}{\partial t} - 2D\Delta G = 2\lambda C \delta(\xi) \quad (32)$$

where $\Delta = \nabla^2$ is the Laplacian operator. We therefore have

$$\mathcal{L}G(\xi, t) = 2\lambda C \delta(\xi) \quad (33)$$

where \mathcal{L} is the linear differential operator $\partial_t - 2D\Delta$.

Using the Green's function theory, we know that $G(y) = \int H(y, s)2\lambda C \delta(s)ds$ where $H(y, s) = H(y - s)$ is the Green kernel (heat kernel). We can therefore write

$$\begin{aligned} G(\xi, t) &= 2\lambda C \int_{\mathbb{R}^3} \int_0^t H(\xi - \xi', t') \delta(\xi') d\xi' dt' \\ \Leftrightarrow G(\xi, t) &= 2\lambda C \int_0^t H(\xi, t') dt'. \end{aligned} \quad (34)$$

A solution for the Green's function using $\mathcal{L} = \partial_t - 2D\Delta$ in three dimensions is $H(r, t) = \left(\frac{1}{8\pi Dt}\right)^{3/2} \exp\left(\frac{-r^2}{8Dt}\right)$. $G(r, t)$ can then be computed as

$$G(r, t) = 2\lambda C \left(\frac{-\text{erf}\left(\frac{r}{\sqrt{8Dt}}\right)}{8\pi Dr} + K \right) \quad (35)$$

⁵²³ where erf is the error function. Using $G(r, 0) = C^2$ and $\lim_{x \rightarrow +\infty} \text{erf}(x) = 1$ in Eq. 35,

$$\begin{aligned} C^2 &= 2\lambda C \left(\frac{1}{8\pi Dr} + K \right) \\ \Leftrightarrow \frac{C}{2\lambda} - \frac{1}{8\pi Dr} &= K. \end{aligned} \quad (36)$$

⁵²⁴ We can finally compute $G(r, t)$:

$$\begin{aligned} G(r, t) &= 2\lambda C \left(-\frac{\text{erf}\left(\frac{r}{\sqrt{8Dt}}\right)}{8\pi Dr} + \frac{C}{2\lambda} + \frac{1}{8D\pi r} \right) \\ &= \frac{\lambda C}{4\pi Dr} \left\{ 1 - \text{erf}\left(\frac{r}{\sqrt{8Dt}}\right) \right\} + C^2 \\ \Leftrightarrow g(r, t) &= \frac{\lambda}{4D\pi r C} \left\{ 1 - \text{erf}\left(\frac{r}{\sqrt{8Dt}}\right) \right\} + 1. \end{aligned} \quad (37)$$

525 Proof of Eq. 8 and Eq. 9

⁵²⁶ We can integrate thepcf formula to compute Ripley's K -function, as $g(r) = \frac{K'(r)}{4\pi r^2}$.

⁵²⁷ **Steady-state solution** From Eq. 30,

$$K(\rho) = 4\pi \int_0^\rho r^2 + \frac{\lambda}{2\pi C} \left[\frac{r}{2D} + \frac{\sqrt{\gamma}r^2 \arctan\left(\frac{\sqrt{\gamma}r}{\sqrt{2D}}\right)}{2\sqrt{2D}\sqrt{D}} - \frac{\sqrt{\gamma}\pi r^2}{4\sqrt{2D}\sqrt{D}} \right] dr. \quad (38)$$

⁵²⁸ We define $A = \int_0^\rho r^2 dr$, $B = \int_0^\rho \frac{r}{2D} dr$, $C = \int_0^\rho r^2 \arctan\left(\frac{\sqrt{\gamma}r}{\sqrt{2D}}\right) dr$ and $E = \int_0^\rho \frac{\sqrt{\gamma}\pi r^2}{4\sqrt{2D}\sqrt{D}} dr$.

$$\begin{aligned} A &= \frac{1}{3}\rho^3. \\ B &= \frac{\rho^2}{4D}. \\ E &= \frac{\sqrt{\gamma}\pi\rho^3}{12\sqrt{2D}\sqrt{D}}. \end{aligned} \quad (39)$$

⁵²⁹ We can also compute $C = \int_0^\rho r^2 \arctan\left(\frac{\sqrt{\gamma}r}{\sqrt{2D}}\right) dr$. We first change variable, with $u = \frac{r}{\sqrt{2D}}$,
⁵³⁰ $dr = \sqrt{2D}du$, and obtain

$$C = (2D)^{3/2} \int_0^{\rho/\sqrt{2D}} u^2 \arctan(\sqrt{\gamma}u) du. \quad (40)$$

⁵³¹ We can integrate by parts, with $f = \arctan(\sqrt{\gamma}u)$ and $g' = u^2$, which leads to

$$C = (2D)^{3/2} \left(\frac{\rho^3}{3(2D)^{3/2}} \arctan\left(\sqrt{\frac{\gamma}{2D}}\rho\right) - \frac{\sqrt{\gamma}}{3} \int_0^{\rho/\sqrt{2D}} \frac{u^3}{(\gamma u^2 + 1)} du \right). \quad (41)$$

⁵³² We then substitute $v = \gamma u^2 + 1$, $du = \frac{1}{2\gamma u} dv$, and have

$$\begin{aligned} \int_0^{\rho/\sqrt{2D}} \frac{u^3}{(\gamma u^2 + 1)} du &= \frac{1}{2\gamma^2} \int_1^{\gamma\rho^2/2D+1} \frac{v-1}{v} dv \\ &= \frac{1}{2\gamma^2} \int_1^{\gamma\rho^2/2D+1} 1 - \frac{1}{v} dv \\ &= \frac{1}{2\gamma^2} \left(\gamma \frac{\rho^2}{2D} - \log\left(\gamma \frac{\rho^2}{2D} + 1\right) \right). \end{aligned} \quad (42)$$

⁵³³ Going back to C, we obtain

$$\begin{aligned} C &= \frac{\rho^3 \arctan(\sqrt{\frac{\gamma}{2D}} \rho)}{3} - (2D)^{3/2} \frac{\sqrt{\gamma}}{3} \frac{1}{2\gamma^2} \left(\frac{\gamma}{2D} \rho^2 - \log\left(\gamma \frac{\rho^2}{2D} + 1\right) \right) \\ &= \frac{\rho^3 \arctan(\sqrt{\frac{\gamma}{2D}} \rho)}{3} - \frac{\sqrt{2D}}{6\sqrt{\gamma}} \rho^2 + \frac{\sqrt{2D}^{3/2}}{3\gamma^{3/2}} \log\left(\gamma \frac{\rho^2}{2D} + 1\right). \end{aligned} \quad (43)$$

⁵³⁴ Combining all equations,

$$\begin{aligned} K(\rho) &= \frac{4}{3}\pi\rho^3 + \frac{2\lambda}{C} \left(\frac{\rho^2}{4D} + \frac{\sqrt{\gamma}\rho^3 \arctan(\sqrt{\frac{\gamma}{2D}} \rho)}{6\sqrt{2D}^{3/2}} - \frac{\rho^2}{12D} + \frac{\log\left(\gamma \frac{\rho^2}{2D} + 1\right)}{6\gamma} - \frac{\sqrt{\gamma}\pi\rho^3}{12\sqrt{2D}\sqrt{D}} \right) \\ &= \frac{4}{3}\pi\rho^3 + \frac{\lambda}{3C} \left(\frac{\rho^2}{D} + \frac{\sqrt{\gamma}\rho^3 \arctan(\sqrt{\frac{\gamma}{2D}} \rho)}{\sqrt{2D}^{3/2}} + \frac{\log\left(\gamma \frac{\rho^2}{2D} + 1\right)}{\gamma} - \frac{\sqrt{\gamma}\pi\rho^3}{2\sqrt{2D}\sqrt{D}} \right). \end{aligned} \quad (44)$$

⁵³⁵ Note that in the absence of advection,

$$\begin{aligned} g(r) &= \frac{\lambda}{4\pi CD r} + 1 \\ \Rightarrow K'(r) &= \frac{\lambda r}{CD} + 4\pi r^2 \\ \Leftrightarrow K(r) &= \frac{\lambda r^2}{2CD} + \frac{4}{3}\pi r^3. \end{aligned} \quad (45)$$

⁵³⁶ **Time-dependent solution** In the absence of advection ($U = 0, \gamma = 0$), we need to compute a time-dependent solution. From eq. 37,

$$\begin{aligned} K(\rho) &= \frac{\lambda}{DC} \int_0^\rho r \left\{ 1 - \operatorname{erf}\left(\frac{r}{\sqrt{8Dt}}\right) \right\} + 4\pi r^2 dr \\ &= \frac{\lambda}{CD} \left(\frac{\rho^2}{2} - \int_0^\rho r \times \operatorname{erf}\left(\frac{r}{\sqrt{8Dt}}\right) dr \right) + \frac{4}{3}\pi\rho^3. \end{aligned} \quad (46)$$

⁵³⁸ We first compute the primitive for $\int_0^\rho r \times \operatorname{erf}\left(\frac{r}{\sqrt{8Dt}}\right) dr$. We define $u = \frac{r}{\sqrt{8Dt}}$, $dr = \sqrt{8Dt} du$,
⁵³⁹ then

$$\int_0^\rho r \times \operatorname{erf}\left(\frac{r}{\sqrt{8Dt}}\right) dr = 8Dt \int_0^{\rho/\sqrt{8Dt}} u \times \operatorname{erf}(u) du. \quad (47)$$

⁵⁴⁰ We can integrate by parts, with $f = \operatorname{erf}(u)$ and $g' = u$, and obtain

$$8Dt \int_0^{\rho/\sqrt{8Dt}} u \times \operatorname{erf}(u) du = 8Dt \left(\frac{\rho^2}{2} \frac{1}{8Dt} \operatorname{erf}\left(\frac{\rho}{\sqrt{8Dt}}\right) - \frac{1}{\sqrt{\pi}} \int_0^{\rho/\sqrt{8Dt}} u^2 e^{-u^2} du \right). \quad (48)$$

⁵⁴¹ We integrate by parts again, this time with $f = u$ and $g' = ue^{-u^2}$, which leads to

$$\int u^2 e^{-u^2} du = -\frac{ue^{-u^2}}{2} + \frac{1}{2} \int e^{-u^2} du = -\frac{ue^{-u^2}}{2} + \frac{\sqrt{\pi} \operatorname{erf}(u)}{4}. \quad (49)$$

⁵⁴² If we use Eq. 49 in Eq. 48,

$$\begin{aligned} 8Dt \int_0^{\rho/\sqrt{8Dt}} u \times \operatorname{erf}(u) du &= 8Dt \left(\frac{\rho^2}{2} \frac{1}{8Dt} \operatorname{erf}\left(\frac{\rho}{\sqrt{8Dt}}\right) - \frac{\operatorname{erf}\left(\frac{\rho}{\sqrt{8Dt}}\right)}{4} + \frac{1}{2\sqrt{\pi}} \frac{\rho}{\sqrt{8Dt}} e^{-\frac{\rho^2}{8Dt}} \right) \\ \Leftrightarrow \int_0^{\rho} r \times \operatorname{erf}\left(\frac{r}{\sqrt{8Dt}}\right) dr &= \frac{1}{2} \operatorname{erf}\left(\frac{\rho}{\sqrt{8Dt}}\right) (\rho^2 - 4Dt) + \frac{\sqrt{2Dt}}{\sqrt{\pi}} \rho e^{-\frac{\rho^2}{8Dt}}. \end{aligned} \quad (50)$$

⁵⁴³ We can now compute $K(\rho)$:

$$K(\rho) = \frac{\lambda}{CD} \left(\frac{\rho^2}{2} - \frac{1}{2} \operatorname{erf}\left(\frac{\rho}{\sqrt{8Dt}}\right) (\rho^2 - 4Dt) - \frac{\sqrt{2Dt}\rho}{\sqrt{\pi}} e^{-\frac{\rho^2}{8Dt}} \right) + \frac{4}{3}\pi\rho^3. \quad (51)$$

⁵⁴⁴ References

- ⁵⁴⁵ Adler, P.B., Smull, D., Beard, K.H., Choi, R.T., Furniss, T., Kulmatiski, A., Meiners, J.M.,
⁵⁴⁶ Tredennick, A.T. & Veblen, K.E. (2018). Competition and coexistence in plant communities:
⁵⁴⁷ intraspecific competition is stronger than interspecific competition. *Ecology Letters*,
⁵⁴⁸ 21, 1319–1329.
- ⁵⁴⁹ Arnott, R.N., Cherif, M., Bryant, L.D. & Wain, D.J. (2021). Artificially generated turbulence:
⁵⁵⁰ a review of phycological nanocosm, microcosm, and mesocosm experiments. *Hydrobiologia*,
⁵⁵¹ 848, 961–991.
- ⁵⁵² Arrieta, J., Jeanneret, R., Roig, P. & Tuval, I. (2020). On the fate of sinking diatoms: the
⁵⁵³ transport of active buoyancy-regulating cells in the ocean. *Philosophical Transactions of
⁵⁵⁴ the Royal Society A*, 378, 20190529.
- ⁵⁵⁵ Bainbridge, R. (1957). The size, shape and density of marine phytoplankton concentrations.
⁵⁵⁶ *Biological Reviews*, 32, 91–115.
- ⁵⁵⁷ Barabás, G., Michalska-Smith, M.J. & Allesina, S. (2017). Self-regulation and the stability
⁵⁵⁸ of large ecological networks. *Nature Ecology & Evolution*, 1, 1870–1875.
- ⁵⁵⁹ Barraquand, F. & Murrell, D.J. (2012). Evolutionarily stable consumer home range size in
⁵⁶⁰ relation to resource demography and consumer spatial organization. *Theoretical Ecology*,
⁵⁶¹ 5, 567–589.

- 562 Barton, A.D., Ward, B.A., Williams, R.G. & Follows, M.J. (2014). The impact of fine-scale
563 turbulence on phytoplankton community structure. *Limnology and Oceanography: Fluids*
564 and Environments
- 565 Bec, B., Collos, Y., Vaquer, A., Mouillot, D. & Souchu, P. (2008). Growth rate peaks at inter-
566 mediate cell size in marine photosynthetic picoeukaryotes. *Limnology and Oceanography*,
567 53, 863–867.
- 568 Benczik, I.J., Károlyi, G., Scheuring, I. & Tél, T. (2006). Coexistence of inertial competitors
569 in chaotic flows. *Chaos*, 16, 043110.
- 570 Birch, D.A. & Young, W.R. (2006). A master equation for a spatial population model with
571 pair interactions. *Theoretical Population Biology*, 70, 26–42.
- 572 Bissinger, J.E., Montagnes, D.J.S., Harples, J. & Atkinson, D. (2008). Predicting marine
573 phytoplankton maximum growth rates from temperature: improving on the Eppley curve
574 using quantile regression. *Limnology and Oceanography*, 53, 487–493.
- 575 Bolker, B.M. & Pacala, S.W. (1999). Spatial moment equations for plant competition: under-
576 standing spatial strategies and the advantages of short dispersal. *The American Naturalist*,
577 153, 575–602.
- 578 Borgnino, M., Arrieta, J., Boffetta, G., De Lillo, F. & Tuval, I. (2019). Turbulence induces
579 clustering and segregation of non-motile, buoyancy-regulating phytoplankton. *Journal of*
580 *the Royal Society Interface*, 16, 20190324.
- 581 Bouderbala, I., El Saadi, N., Bah, A. & Auger, P. (2018). A 3D individual-based model
582 to study effects of chemotaxis, competition and diffusion on the motile-phytoplankton
583 aggregation. *Acta Biotheoretica*, 66, 257–278.
- 584 Breier, R.E., Lalescu, C.C., Waas, D., Wilczek, M. & Mazza, M.G. (2018). Emergence of
585 phytoplankton patchiness at small scales in mild turbulence. *Proceedings of the National*
586 *Academy of Sciences*, 115, 12112–12117.
- 587 Chesson, P. (2018). Updates on mechanisms of maintenance of species diversity. *Journal of*
588 *Ecology*, 106, 1773–1794.
- 589 Detto, M. & Muller-Landau, H.C. (2016). Stabilization of species coexistence in spatial mod-
590 els through the aggregation-segregation effect generated by local dispersal and nonspecific
591 local interactions. *Theoretical Population Biology*, 112, 97–108.

- 592 Doubell, M.J., Seuront, L., Seymour, J.R., Patten, N.L. & Mitchell, J.G. (2006). High-
593 resolution fluorometer for mapping microscale phytoplankton distributions. *Applied and*
594 *Environmental Microbiology*, 72, 4475–4478.
- 595 Dusenberry, D. (2009). *Living at the microscale*. Harvard University Press.
- 596 Edwards, K.F. (2019). Mixotrophy in nanoflagellates across environmental gradients in the
597 ocean. *Proceedings of the National Academy of Sciences*, p. 201814860.
- 598 Einstein, A. (1905). Über die von der molekularkinetischen theorie der wärme geforderte
599 bewegung von in ruhenden flüssigkeiten suspendierten teilchen. *Annalen der physik*, 4.
- 600 Estrada, M., Alcaraz, M. & Marrasé, C. (1987). Effects of turbulence on the composition
601 of phytoplankton assemblages in marine microcosms. *Marine Ecology Progress Series*, 38,
602 267–281.
- 603 Field, C.B., Behrenfeld, M.J., Randerson, J.T. & Falkowski, P. (1998). Primary production
604 of the biosphere: integrating terrestrial and oceanic components. *Science*, 281, 237–240.
- 605 Font-Muñoz, J.S., Jeanneret, R., Arrieta, J., Anglès, S., Jordi, A., Tuval, I. & Basterretxea,
606 G. (2019). Collective sinking promotes selective cell pairing in planktonic pennate diatoms.
607 *Proceedings of the National Academy of Sciences*, 116, 15997–16002.
- 608 Font-Muñoz, J.S., Jordi, A., Tuval, I., Arrieta, J., Anglès, S. & Basterretxea, G. (2017).
609 Advection by ocean currents modifies phytoplankton size structure. *Journal of the Royal*
610 *Society Interface*, 14, 20170046.
- 611 Haegeman, B. & Rapaport, A. (2008). How flocculation can explain coexistence in the
612 chemostat. *Journal of Biological Dynamics*, 2, 1–13.
- 613 Hellweger, F.L. & Bucci, V. (2009). A bunch of tiny individuals – individual-based modeling
614 for microbes. *Ecological Modelling*, 220, 8–22.
- 615 Huisman, J. & Weissing, F.J. (1999). Biodiversity of plankton by species oscillations and
616 chaos. *Nature*, 402, 407–410.
- 617 Hutchinson, G.E. (1961). The paradox of the plankton. *The American Naturalist*, 95, 137–
618 145.
- 619 Illian, J., Penttinen, A., Stoyan, H. & Stoyan, D. (2008). *Statistical analysis and modelling*
620 *of spatial point patterns*. vol. 70. John Wiley & Sons.

- 621 Jumars, P.A., Deming, J., Hill, P., Karp-Boss, L., Yager, P. & Dade, W. (1993). Physical
622 constraints on marine osmotrophy in an optimal foraging context. *Marine Microbial Food*
623 *Webs*, 7, 121–159.
- 624 Karp-Boss, L., Boss, E. & Jumars, P.A. (1996). Nutrient fluxes to planktonic osmotrophs in
625 the presence of fluid motion. *Oceanography and Marine Biology: An Annual Review*, 34,
626 71–107.
- 627 Kiørboe, T., Andersen, K.P. & Dam, H.G. (1990). Coagulation efficiency and aggregate
628 formation in marine phytoplankton. *Marine Biology*, 107, 235–245.
- 629 Kraichnan, R.H. (1974). Convection of a passive scalar by a quasi-uniform random straining
630 field. *Journal of Fluid Mechanics*, 64, 737–762.
- 631 Law, R., Murrell, D.J. & Dieckmann, U. (2003). Population growth in space and time: spatial
632 logistic equations. *Ecology*, 84, 252–262.
- 633 Leonard, C.L., Bidigare, R.R., Seki, M.P. & Polovina, J.J. (2001). Interannual mesoscale
634 physical and biological variability in the North Pacific Central Gyre. *Progress in Oceanog-*
635 *rphy*, 49, 227–244.
- 636 Levine, J.M. & HilleRisLambers, J. (2009). The importance of niches for the maintenance
637 of species diversity. *Nature*, 461, 254–257.
- 638 Li, L. & Chesson, P. (2016). The effects of dynamical rates on species coexistence in a
639 variable environment: the paradox of the plankton revisited. *The American Naturalist*,
640 188, E46–E58.
- 641 MacArthur, R. & Levins, R. (1964). Competition, habitat selection and character displace-
642 ment in a patchy environment. *Proceedings of the National Academy of Sciences*, 51,
643 1207–1210.
- 644 Martin, A.P. (2003). Phytoplankton patchiness: the role of lateral stirring and mixing.
645 *Progress in Oceanography*, 57, 125–174.
- 646 Murrell, D. (2005). Local spatial structure and predator-prey dynamics: counterintuitive
647 effects of prey enrichment. *The American Naturalist*, 166, 354–367.
- 648 Ngan, K. & Vanneste, J. (2011). Scalar decay in a three-dimensional chaotic flow. *Physical*
649 *Review E*, 83, 056306.

- 650 North, A. & Ovaskainen, O. (2007). Interactions between dispersal, competition, and land-
651 scape heterogeneity. *Oikos*, 116, 1106–1119.
- 652 Peters, F. & Marrasé, C. (2000). Effects of turbulence on plankton: an overview of experi-
653 mental evidence and some theoretical considerations. *Marine Ecology Progress Series*, 205,
654 291–306.
- 655 Picoche, C. & Barraquand, F. (2019). How self-regulation, the storage effect, and their
656 interaction contribute to coexistence in stochastic and seasonal environments. *Theor Ecol*,
657 12, 489–500.
- 658 Picoche, C. & Barraquand, F. (2020). Strong self-regulation and widespread facilitative
659 interactions in phytoplankton communities. *Journal of Ecology*, 108, 2232–2242.
- 660 Picoche, C., Young, W.R. & Barraquand, F. (2022). [Re] Reproductive pair correlations and
661 the clustering of organisms. *ReScience C*, 8.
- 662 Pierrehumbert, R.T. (1994). Tracer microstructure in the large-eddy dominated regime.
663 *Chaos, Solitons & Fractals*, 4, 1091–1110.
- 664 Plank, M.J. & Law, R. (2015). Spatial point processes and moment dynamics in the life
665 sciences: a parsimonious derivation and some extensions. *Bulletin of Mathematical Biology*,
666 77, 586–613.
- 667 Prairie, J.C., Sutherland, K.R., Nickols, K.J. & Kaltenberg, A.M. (2012). Biophysical inter-
668 actions in the plankton: a cross-scale review. *Limnology and Oceanography: Fluids and*
669 *Environments*, 2, 121–145.
- 670 Record, N.R., Pershing, A.J. & Maps, F. (2014). The paradox of the “paradox of the plank-
671 ton”. *ICES Journal of Marine Science*, 71, 236–240.
- 672 REPHY (2017). *REPHY dataset - French Observation and Monitoring program*
673 *for Phytoplankton and Hydrology in coastal waters. 1987-2016 Metropolitan data.*
674 <https://www.seanoe.org/data/00361/47248/>.
- 675 Reynolds, C.S. (2006). *The ecology of phytoplankton*. Cambridge University Press.
- 676 Schippers, P., Verschoor, A.M., Vos, M. & Mooij, W.M. (2001). Does “supersaturated coex-
677 istence” resolve the “paradox of the plankton”? *Ecology Letters*, 4, 404–407.
- 678 Seymour, J.R., Amin, S.A., Raina, J.B. & Stocker, R. (2017). Zooming in on the phycosphere:
679 the ecological interface for phytoplankton–bacteria relationships. *Nature Microbiology*, 2,
680 17065.

- 681 Stocker, R. (2012). Marine microbes see a sea of gradients. *Science*, 338, 628–633.
- 682 Widdicombe, C. & Harbour, D. (2021). Phytoplankton taxonomic abundance and biomass
683 time-series at Plymouth Station L4 in the Western English Channel, 1992–2020.
- 684 Wiegand, T., Gunatilleke, C.V.S., Gunatilleke, I.A.U.N. & Huth, A. (2007). How individual
685 species structure diversity in tropical forests. *Proceedings of the National Academy of
686 Sciences*, 104, 19029–19033.
- 687 Young, W.R., Roberts, A.J. & Stuhne, G. (2001). Reproductive pair correlations and the
688 clustering of organisms. *Nature*, 412, 328–331.